SAND21XX-XXXXR
LDRD PROJECT NUMBER: 226346
LDRD PROJECT TITLE: Quantification of morphological change in materials based on image data utilizing machine learning techniques

PROJECT TEAM MEMBERS: Ariana Beste/7555, Dan Bolintineanu/1516, Dan Bufford/7555

ABSTRACT:

Computed tomography (CT) resolution has become high enough to monitor morphological changes due to aging in materials in long-term applications. We explored the utility of the critic of a generative adversarial network (GAN) to automatically detect such changes. The GAN was trained with images of pristine Pharmatose, which is used as a surrogate energetic material. It is important to note that images of the material with altered morphology were only used during the test phase. The GAN-generated images visually reproduced the microstructure of Pharmatose well, although some unrealistic particle fusion was seen. Calculated morphological metrics (volume fraction, interfacial line length, and local thickness) for the synthetic images also showed good agreement with the training data, albeit with signs of mode collapse in the interfacial line length. While the critic exposed changes in particle size, it showed limited ability to distinguish images by particle shape. The detection of shape differences was also a more challenging task for the selected morphological metrics that related to energetic material performance. We further tested the critic with images of aged Pharmatose. Subtle changes due to aging are difficult for the human analyst to detect. Both critic and morphological metrics analysis showed image differentiation.

INTRODUCTION AND EXECUTIVE SUMMARY OF RESULTS:

Computed tomography (CT) is increasingly used for quality control of manufactured parts to detect production defects. Although high-resolution is not necessary for these applications, in recent years, laboratory CT instruments that yield images with voxel sizes smaller than one micrometer have become available, allowing the study of material microstructure. In particular, we are interested in the detection of morphological changes that may occur due to material aging in long-term applications. Since a single CT scan produces on the order of a thousand images, an automated analysis technique is highly desirable. In addition, a quantitative measure of morphological material changes would enable the discovery of aging trends based on image data. Traditionally, morphological analysis of material image data is performed by identifying relevant descriptors, typically after image segmentation. These morphological descriptors encompass single-point metrics, spatial correlations, size distributions, regional statistics, topology measures, and more. [1] Their interpretability provides an intuitive understanding of material morphology and structure/property relationships; [2] however, their predefined functional form and low dimensionality prevents a comprehensive description of complex morphologies and interdependencies.

Sandia National Laboratories is a multimission laboratory managed and operated by National Technology and Engineering Solutions of Sandia, LLC, a wholly owned subsidiary of Honeywell International, Inc., for the U.S. Department of Energy's National Nuclear Security Administration under contract DE-NA-0003525.

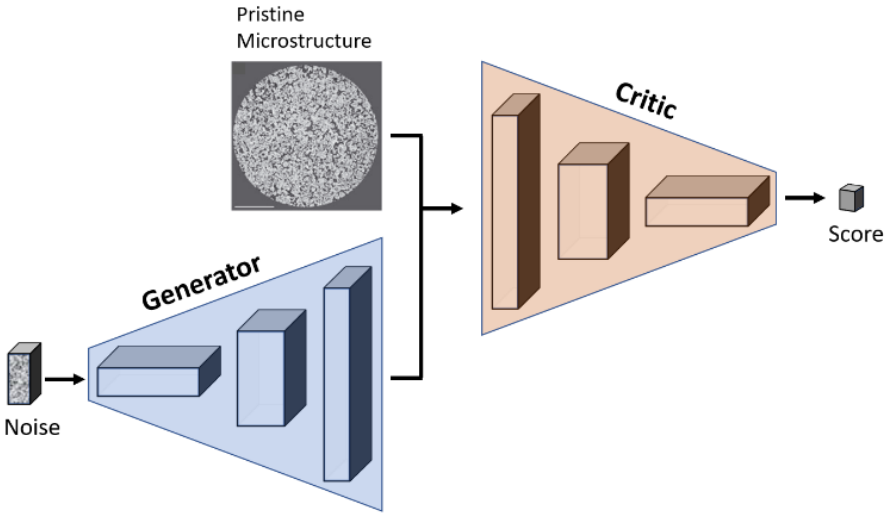

Scheme 1. General structure of a Wasserstein Generative Adversarial Network (WGAN).

Within the field of computer vision, convolutional neural networks (CNN) have been developed to perform image analysis without imposing underlying probability distributions a priori and without the need for simplified metrics. [3] An example of a CNN developed to learn a probability distribution from training images for the purpose of generating more images from the learned distribution is the generative adversarial network (GAN). [4] It provides an efficient sampling method for high-dimensional and intractable density functions. GANs consist of two competing subnetworks: a generator whose role it is to generate samples of the unknown density and a discriminator that tries to distinguish between real and synthetic images created by the generator. Recently, GANs have been used to generate synthetic microstructure images of diverse materials (natural stone, lithium-ion battery cathodes, solid oxide fuel cell anodes, aluminum foam, High Melting eXplosive) trained on SEM and CT images. [5-10] In addition to visual verification of the synthetic realizations, the authors showed that the underlying distributions of morphological descriptors (effective porosity, volume fraction, particle size, interfacial area, void properties, two-point correlation function, etc.) were reproduced and that simulation output (electrochemical performance, [8] reactive dynamics, [9] and flow simulations [7]) of real versus generated microstructures was comparable.

While previous work utilizes the ability of the generator subnetwork to learn and generate realistic representations of material microstructure from SEM and CT images, to our knowledge, the capability of the discriminator has not been exploited so far. However, the discriminator is trained in conjunction with the generator to compute the probability that the material morphology captured in a query image is sampled from the learned distribution. If the distribution is learned from pristine material, the discriminator is able to distinguish between pristine and altered material.

The particular GAN implementation we used was a Wasserstein GAN (WGAN). [11] In contrast to the traditional GAN implementation, [4] the WGAN implements the Wasserstein loss as a measure of the distance between probability distributions. In the context of a WGAN, the discriminator is called a critic, which assigns, instead of a probability, a score to the realness or fakeness of a given image. The general structure of a WGAN is given in **Computed tomography** (CT) is increasingly used for quality control of manufactured parts to detect production defects. Although high-resolution is not necessary for these applications, in recent years, laboratory CT instruments that yield images with voxel sizes smaller than one micrometer have become available, allowing the study of material microstructure. In particular, we are interested in the detection of morphological changes that may occur due to material aging in long-term applications. Since a single CT scan produces on the order of a thousand images, an automated analysis technique is highly desirable. In addition, a quantitative measure of morphological material changes would enable the discovery of aging trends based on image data.
Traditionally, morphological analysis of material image data is performed by identifying relevant descriptors, typically after image segmentation. These morphological descriptors encompass single-point metrics, spatial correlations, size distributions, regional statistics, topology measures, and more. [1] Their interpretability provides an intuitive understanding of material morphology and structure/property relationships; [2] however, their predefined functional form and low dimensionality prevents a comprehensive description of complex morphologies and interdependencies.

Scheme 1. After training, we can use the critic as a one-class classifier, [12] where images of the pristine material are in-class images. When the critic is tested with images of potentially altered material, its scores are a measure of the difference between test images and images of the pristine material. Application of the Wasserstein loss results in more stable training and larger output variability; however, reminiscent of small microstructure variations observed in other work, [5, 7] the WGAN is able to learn average structures better than outliers. [8]

Here, we tested the utility of the trained critic to distinguish between CT images of pristine Pharmatose ® (pharmaceutical a-lactose monohydrate produced by DFE Pharma, Goch, Germany) and images of Pharmatose with altered morphology. Pharmatose was used as a surrogate for energetic materials. The microstructure of Pharmatose was well reproduced in the images generated by the network, although occasional, unrealistic particle fusion occurred. We calculated morphological metrics for generated and real images focusing on metrics that relate to energetic material performance. Overall, we found good agreement, but observed signs of mode collapse. The trained critic was presented with three different test sets. Test set 1 contained images of Pharmatose with different particle sizes than in the images the network was trained on. The critic detected changed morphology. Score ordering was consistent with morphological metric analysis. Test set 2 consisted of transformed training images, where the particle shape was distorted. While it was easy for the human analyst to visually distinguish these particle shape differences from the training images, critic scores did not reflect that. Likewise, the particle shape changes did not

significantly influence morphological metrics relating to performance. Test set 3 included images of aged Pharmatose. Visually, the aged images were difficult to differentiate from pristine data. However, critic as well as morphological metric analysis detected change.

DETAILED DESCRIPTION OF RESEARCH AND DEVELOPMENT AND METHODOLOGY:

Network Description

Details of the network implementation are given elsewhere. [8] The generator input is a vector of random noise, which is fully connected to the first layer. The following layers are up-sampling, convolutional, and batch normalization layers, including four convolutional layers with ReLu activation yielding the output image. The critic takes that image as an input. The critic consists of seven convolutional layers with LeakyReLu activation and a single connected layer to produce the critic score. The learning rate was adjusted during training depending on observed oscillations in the loss function. The number of filters per convolutional layer can conveniently be set as an input parameter. We used two settings: In setting 1, the generator has 256-128-64-32 filters in consecutive convolutional layers and the critic has 32-32-64-64-128-128-256. Network training and testing was performed on a Nvidia V100 (Volta) GPU with 32 GB RAM. For filter setting 1, network training with 512×512 pixel images was memory limited. In setting 2, we used a reduced number of filters for the generator of 128-64-32-16 and for the critic of 16-16-32-32-64-64-128 to speed up training.

Image Data

Pharmatose has been used in our laboratory as a highly compactable surrogate for energetic materials. It is readily available for purchase at varying degrees of fineness; Pharmatose 60M, 100M, and 200M have nominal mean particle diameters of 280, 150, and 40 μm, respectively. Pharmatose powder was placed in cylindrical aging vehicles and scanned using a Zeiss Xradia 520 Versa operated at 40 kV for training set 1 and 60 kV for all other scans. Scans yielded a stack of tiff images (x/y plane) along the length of the cylinder (z-axes) with pixel size in the range of 1 to 1.5 μm as described below.

Training Sets

We used two different training sets. Training set 1 was obtained from a CT scan of Pharmatose 60M, consisting of 2,026 images, each 2048×2004 pixels with a pixel length of 1.55 μm. This set was used to train the network for subsequent critic interrogation with test sets 1 and 2. Since no aged data was available for this particular Pharmatose batch, we retrained the network with training set 2, which was generated from a CT scan of Pharmatose 100M, consisting of 2,022 images, each 2048×2007 pixels with a pixel length of 1.22 μm. The critic was subsequently tested with test set 3.

Test Set 1

Test set 1 includes images of Pharmatose with varying particle sizes. Pharmatose 60M is the coarsest of the three sizes; Pharmatose 100M is milled to smaller size particles than Pharmatose 60M, and Pharmatose 200M is milled to an even finer size. CT instrument settings to generate test set 1 were the same as for training set 2, resulting in the same image and pixel sizes. Set "Large" was obtained from a CT scan of Pharmatose 60M. The fact that the particles appear larger in test set "Large" than in training set 1, which also consists of images of Pharmatose 60M, is a combination of different CT magnification (which can be scaled for) and varying details in the material specifications. Test set "Medium" is the same as training set 2. Pharmatose 200M was scanned to obtain test set "Small."

Test Set 2

Test set 2 was generated by transforming the images of training set 1 to distort the particle shape. We utilized the Python library Scikit-Image. [13] A swirl was added to create test set "Swirl." The images were remapped into polar coordinate space to obtain test set "Polar," and a sinus wave was superimposed, yielding test set "Wave."

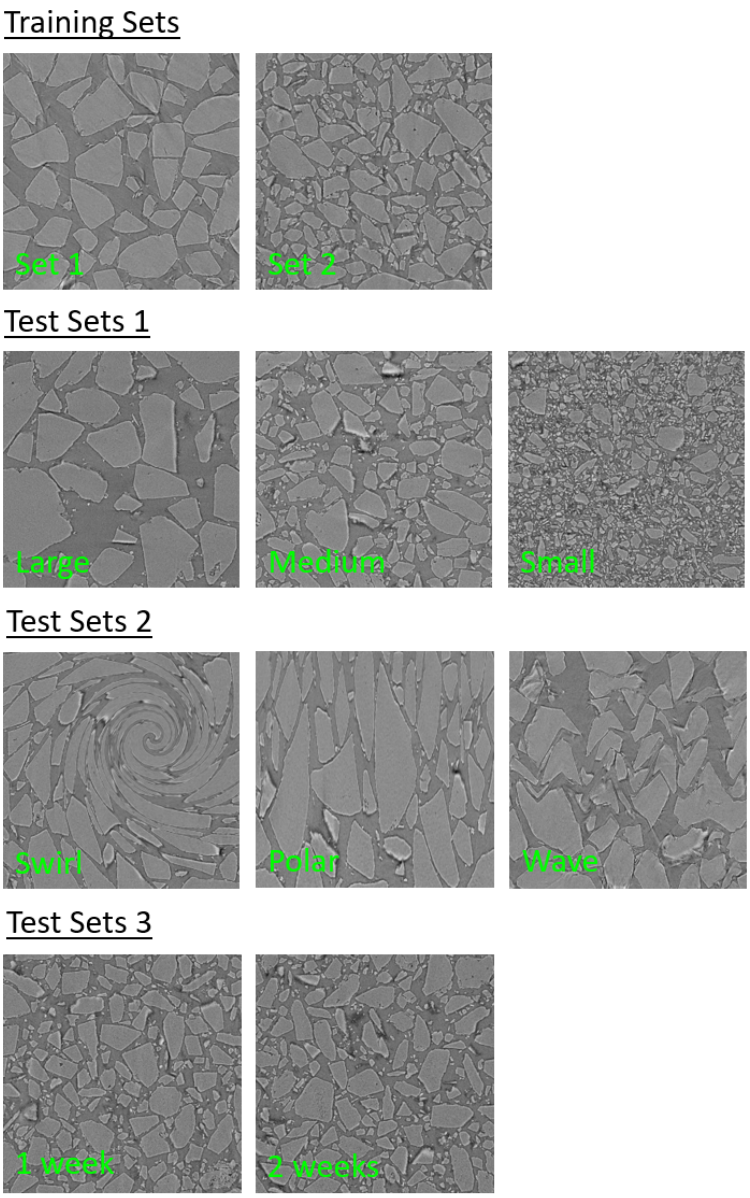

Figure 1. Example images for train and test sets.

Test Set 3

Test set 3 was obtained from aged Pharmatose 100M. Aging vehicles containing Pharmatose 100M were placed in an oven for one week (test set "1 week") and two weeks (test set "2 weeks") at 100°C. Aged Pharmatose was scanned using the same instrument settings as those used for training set 2.

Training and test sets were pre-processed prior to training/testing. The bottom and the top of the aging vehicle were imaged in approximately the first and last 100 images (imaging artifacts may also occur close to the bottom and the top of the container). Images along the z-axes that either showed the aging vehicle or imaging artifacts were removed from the tiff stack. The aging vehicle is visible as a ring in the x/y plane. Images were cropped to 1380×1380 pixels to exclude the container from the images. Further, images were down-sampled to one quarter in image area. Sub-image batches for training and testing were created by randomly rotating and flipping the images and cropping to 512×512 pixel image segments. An example image for each train/test batch is shown in **Figure 1**. Batches of 1,000 images were scored for critic and generator evaluations.

Morphological Metrics

To verify and interpret the network scores, we calculated morphological metrics. We chose to calculate the volume fraction, which relates to the density of the material, and the interfacial line length, which is the two-dimensional equivalent of the specific surface area. Both correlate with performance properties of energetic materials. [14, 15] Further, we calculated the local thickness[16] of the particle phase, which is related to particle size distribution, but does not require segmentation of individual particles.

Prior to morphological metric calculations, the images were segmented into particle and void space. A bilateral filter was applied, followed by a random walker algorithm for segmentation, again utilizing the Scikit-Image library.[8] The calculation of the volume fraction only required counting of void and particle pixels, while the calculation of the interfacial line length was more involved. Splines were used to interpolate a smoothed curve as the interface between two phases. Subsequently, the contour length along that curve was computed and then divided by the total area of the image, resulting in units of voxels^{-1}. We used the PoreSpy library [17] to evaluate the local thickness, which approximates local particle sizes by fitting maximal circles of different sizes into the particle space.

Morphological metrics are reported as averages over 100 test images and 100 generated images.

RESULTS AND DISCUSSION:

Image Generation

Before testing the critic, we verified that the network was generating realistic images of Pharmatose.

Training Set 1

We trained the network with training set 1 and filter setting 1. An example of an image generated from the same random seed vector at different epochs is compared to an example training image (real image) in **Figure 2**. Overall, the microstructure of Pharmatose was well-reproduced by the network; however, some particles had an unrealistic appearance. This can be observed in **Figure 2** and is marked with red arrows. Particle boundaries were not always well-recreated in the synthetic images, resulting in fused particles. This behavior persisted up to high epochs.

Figure 3 a) compares the scores for real images to scores for synthetic images at different epochs using the critic of the respective epoch. While scores for different epochs varied significantly, at each epoch, the critic scored real and synthetic images similarly. Comparing the critic scores for real images at different epochs in **Figure 3 b)**, we find a shift to smaller scores as the number of epochs increases. We note, however, that convergence of the scores with increasing epochs is not necessarily expected because the synthetic images with which the critic trains will change with epoch.

Figure 4 contrasts morphological metrics calculated from synthetic images at different epochs with those calculated from real images. We observed good agreement between the two sets. The volume fraction of the real images appeared to be better reproduced in the synthetic images obtained at higher epochs, while interfacial line length and local thickness showed small fluctuations with epochs above 600. The interfacial line length of the real images exhibited bimodal character. To test if this was the consequence of undersampling, **Figure 4** shows the histograms of the interfacial line length for 100 and 200 real images. The bimodal character was still observable when the interfacial line length is computed for 200 images. This was not reproduced in the generated images. Mode collapse was previously observed for distributions generated by GANs. [18]

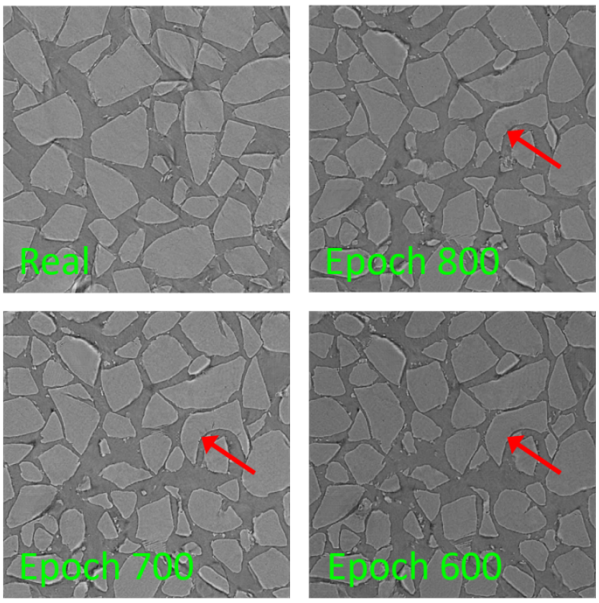

Figure 2. Training set 1: examples of one real and three generated images at different epochs obtained from the same random seed vector; unrealistic, fused particles are highlighted with a red arrow.

For network training with training set 2, we used a reduced number of convolutional filters (filter setting 2). To ensure that this did not skew our results, we retrained the network using training set 1 with filter setting 2. Example images generated by the network and calculated morphological metrics can be found in **Figure 5** and **Figure 6**. Note that epochs are not directly comparable due to learning rate adjustments. Results for filter setting 1 and 2 were very similar.

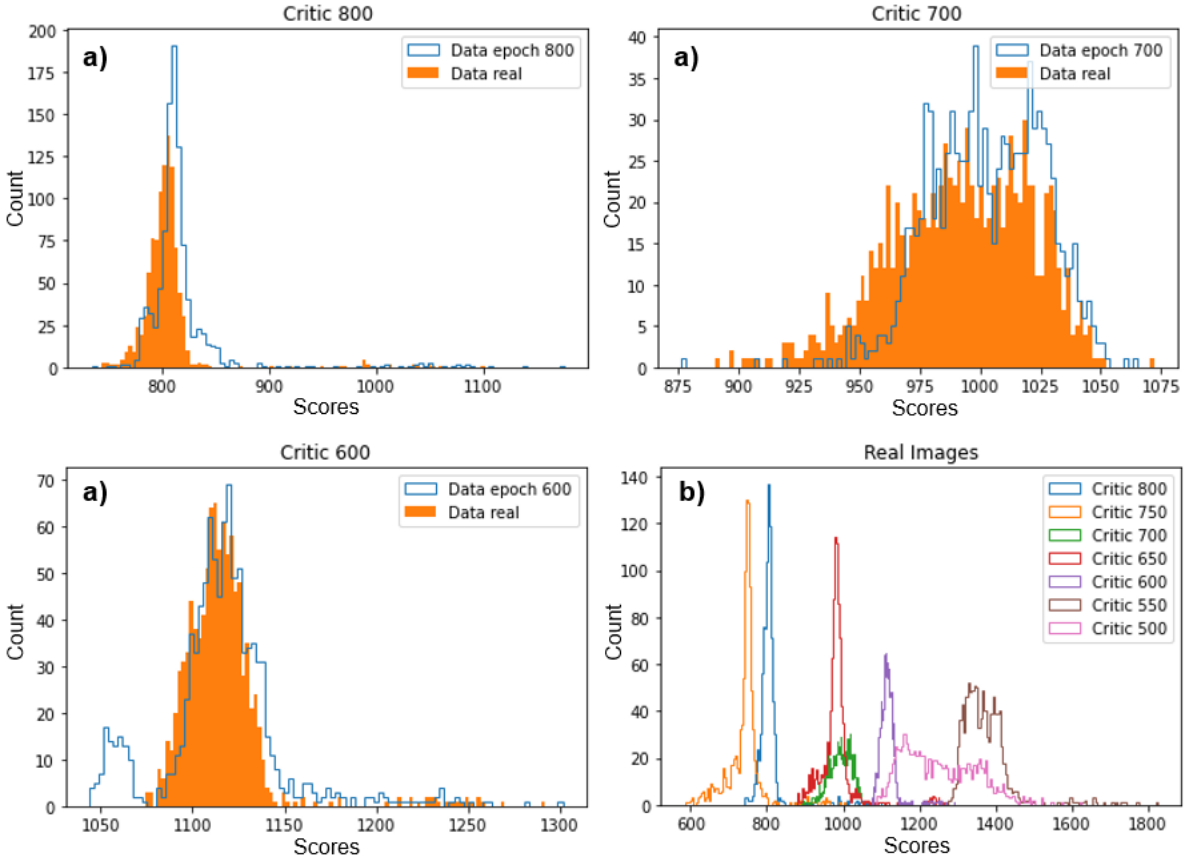

Figure 3. Training set 1: **a)** scores for synthetic images at different epochs compared to scores for real images using the respective critic; **b)** scores for real images using the critic of different epochs (1,000 images were scored per histogram).

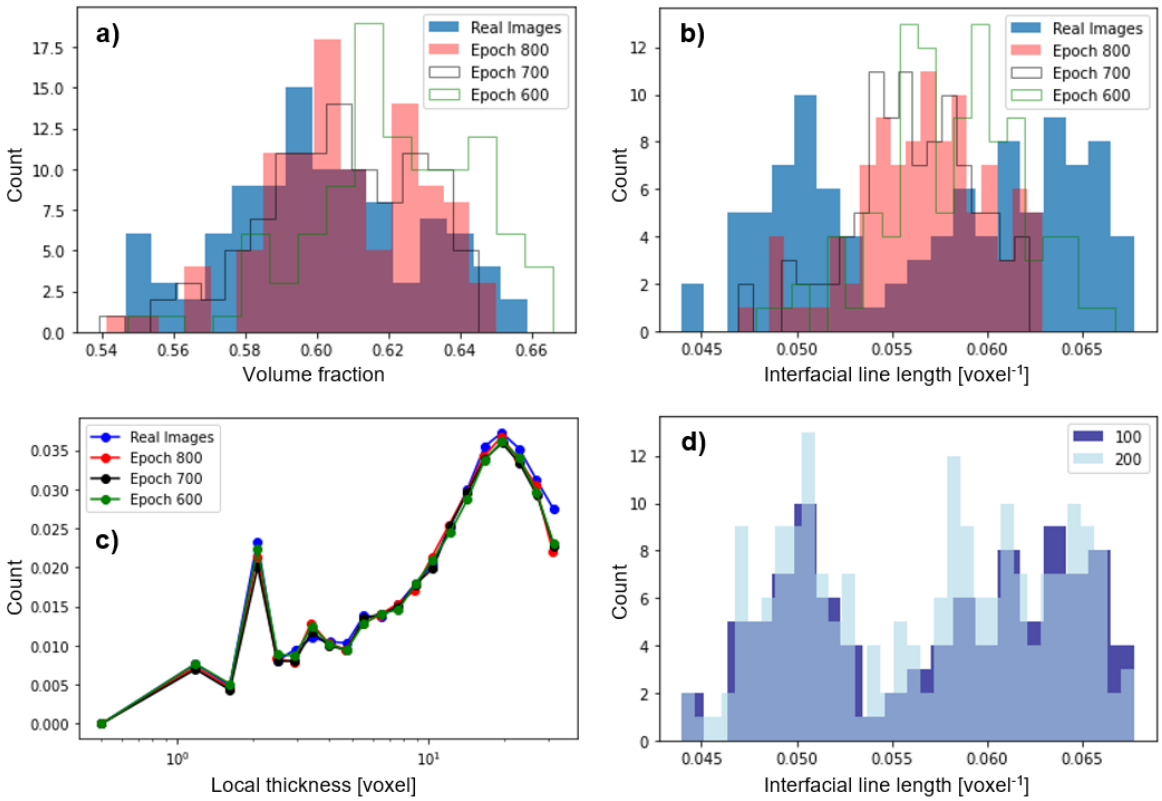

Figure 4. Training set 1: **a)** to **c)** comparison of morphological metrics computed for synthetic images generated at different epochs and for real images (100 images were evaluated); **a)** volume fraction, **b)** interfacial line length, **c)** local thickness; **d)** interfacial line length computed for 100 and 200 real images.

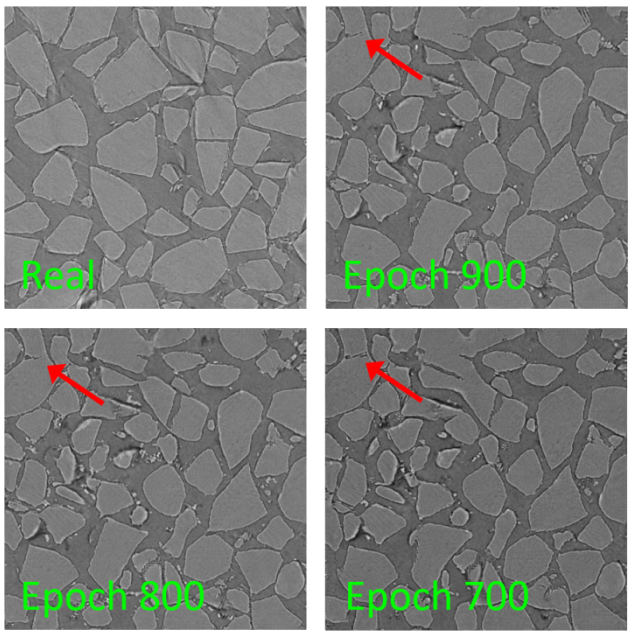

Figure 5. Training set 1: reduced number of filters (filter setting 2); examples of a real and generated images at different epochs obtained from the same random seed vector; unrealistic, fused particles are highlighted with a red arrow.

Training Set 2

We trained the network with training set 2 and filter setting 2. Visual inspection of generated images led to the same conclusion as for training set 1; the microstructure of Pharmatose 100M was well reproduced but some particles appeared to be fused, see **Figure 7**. **Figure 8** compares the critic scores for generated images at different epochs to the scores of real images. As for training set 1, scores tended to get smaller with increasing epochs (although scores are negative for training set 2). The score distributions for the synthetic images were wider compared to the real images. For training set 1, the distribution widths were comparable. The calculation of morphological metrics (volume fraction, interfacial line length, local thickness) yielded similar results for generated and real images, see **Figure 9**.

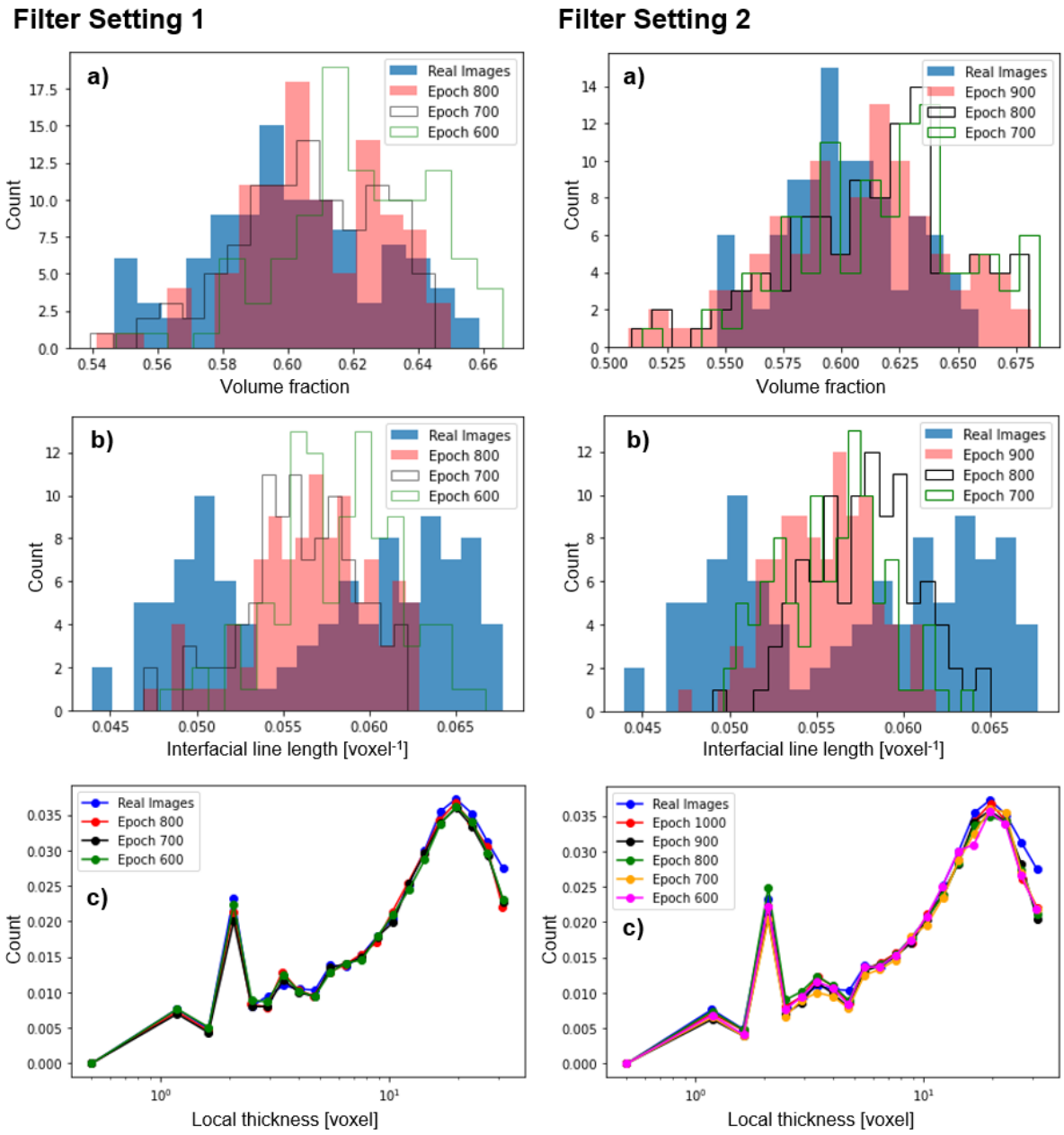

Figure 6. Training set 1: **a)** to **c)** morphological metrics computed for synthetic images generated at different epochs and for real images; **a)** volume fraction, **b)** interfacial line length, **c)** local thickness; network filter setting 1 is compared to a reduced filter setting 2 (100 images were evaluated).

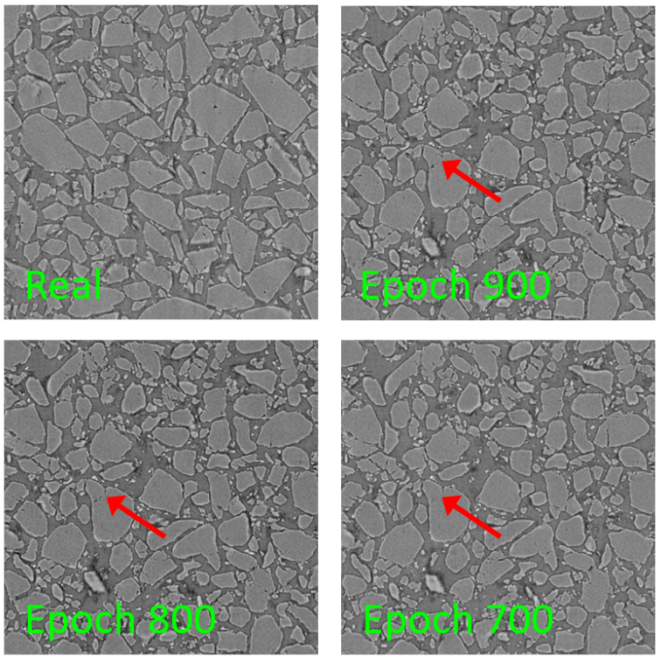

Figure 7. Training set 2: examples of a real and generated images at different epochs obtained from the same random seed vector; unrealistic, fused particles are highlighted with a red arrow.

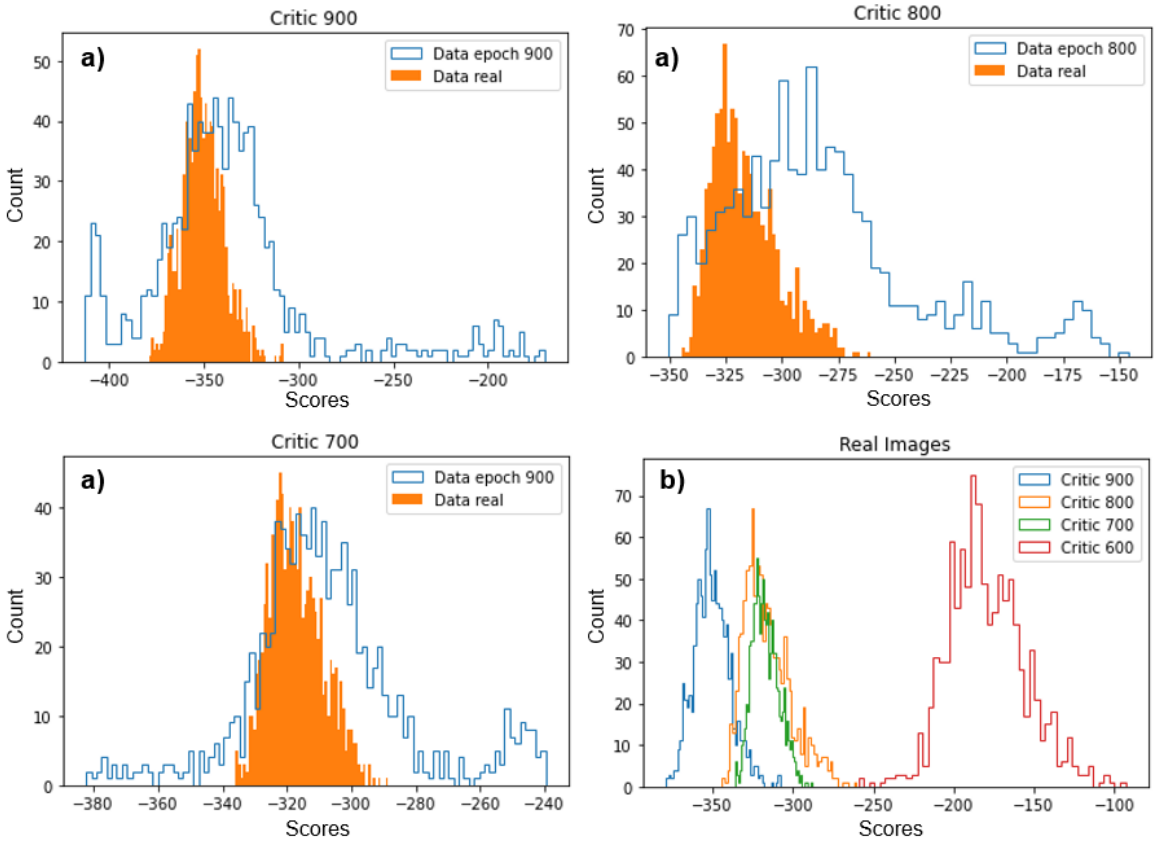

Figure 8. Training set 2: **a)** scores for synthetic images at different epochs compared to scores for real images using the respective critic; **b)** scores for real images using the critic of different epochs (1,000 images were scored per histogram).

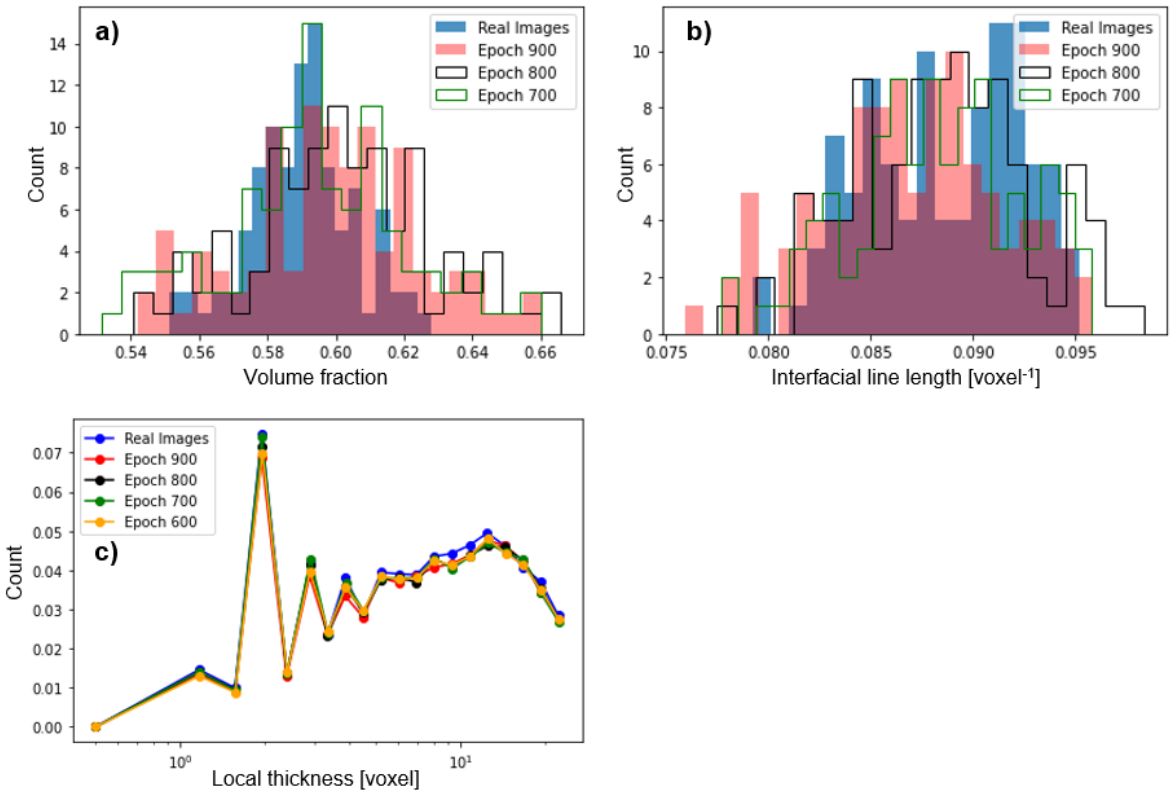

Figure 9. Training set 2: **a)** to **c)** morphological metrics computed for synthetic images generated at different epochs and for real images; **a)** volume fraction, **b)** interfacial line length, **c)** local thickness (100 images were evaluated).

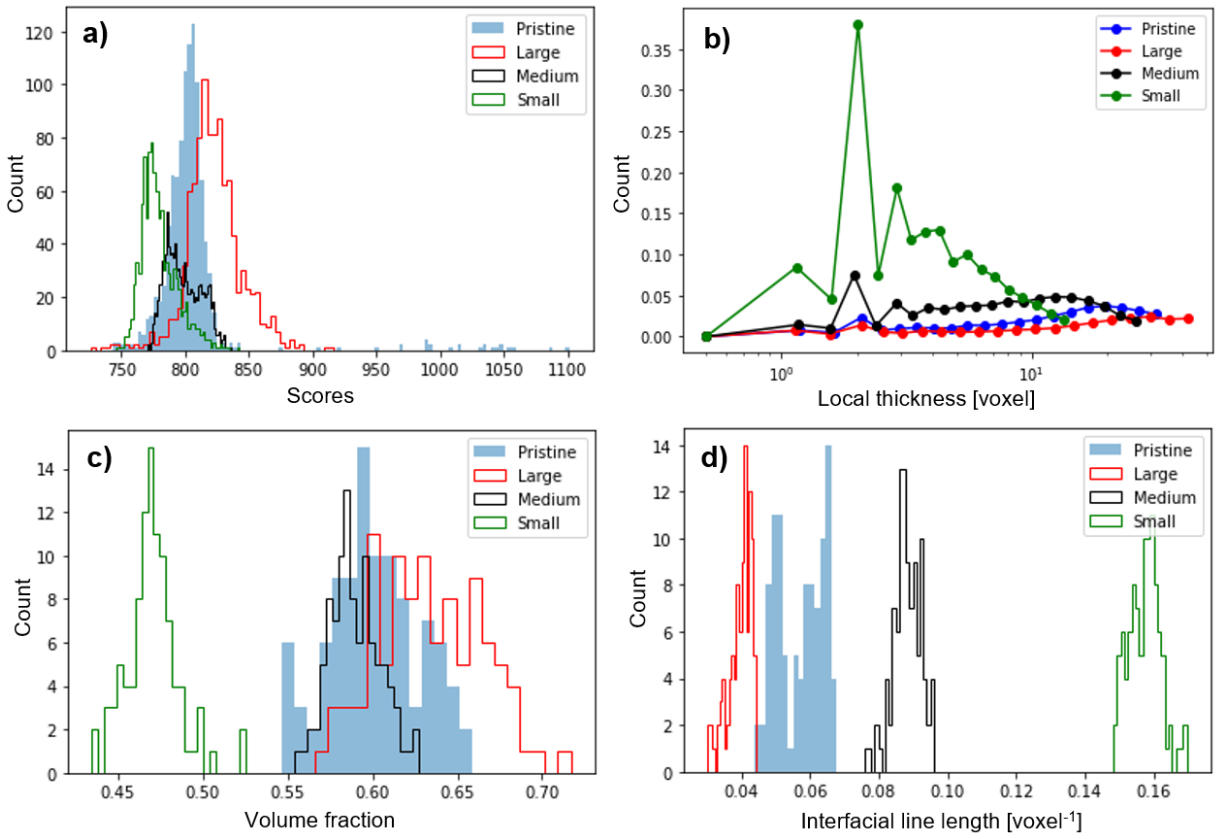

Figure 10. Test set 1: **a)** critic scores, **b)** local thickness, **c)** volume fraction, **d)** interfacial line length computed for training set 1 (Pristine) and for Pharmatose with varying particle sizes; **a)** 1,000 images were evaluated, **b)** to **d)** (100 images were evaluated).

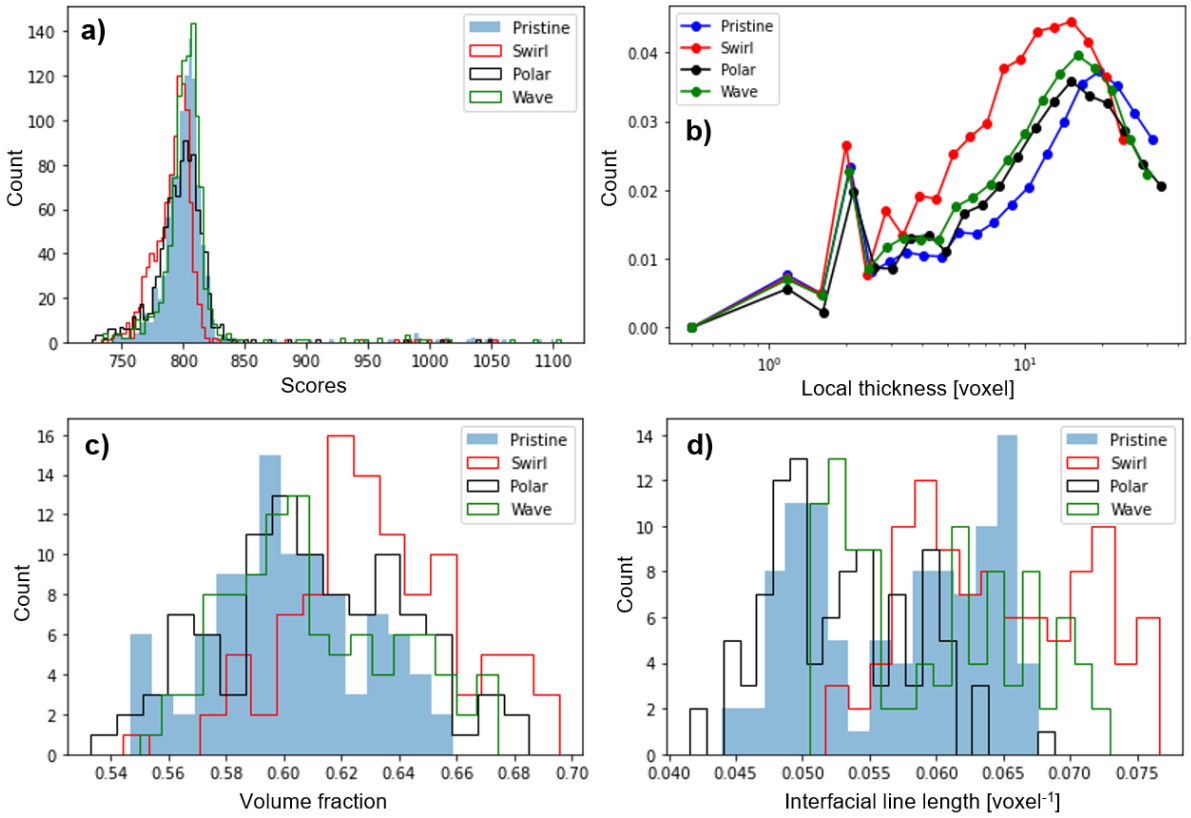

Figure 11. Test set 2: **a)** critic scores, **b)** local thickness, **c)** volume fraction, **d)** interfacial line length computed for training set 1 (Pristine) and for Pharmatose with distorted particle shapes; **a)** 1,000 images were evaluated, **b)** to **d)** 100 images were evaluated.

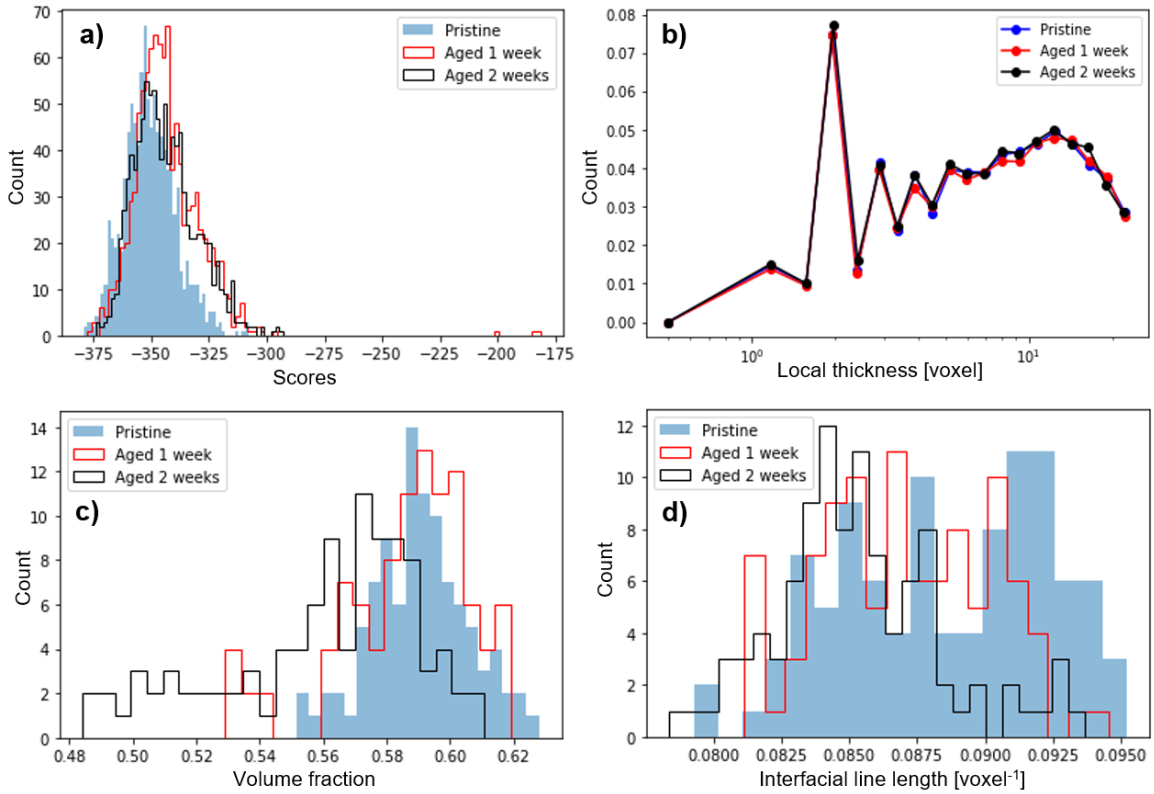

Figure 12. Test set 3: **a)** critic scores, **b)** local thickness, **c)** volume fraction, **d)** interfacial line length computed for training set 2 (Pristine) and for aged Pharmatose; **a)** 1,000 images were evaluated, **b)** to **d)** 100 images were evaluated.

Test Image Evaluation

The critic was presented with three different test sets to probe its ability to distinguish between images that showed a different Pharmatose morphology than that on which it was trained. The critic trained with training set 1 for 800 epochs was used for test sets 1 and 2. The critic trained with training set 2 for 900 epochs was employed for test set 3.

Test Set 1

Figure 10 compares the critic scores for images of pristine Pharmatose (training set 1) to images of Pharmatose with varying particle sizes. The critic scores of the test sets were distinct from the scores of the images of pristine Pharmatose. As the particle size increased, the score distributions shifted to higher scores. The calculated morphological metrics also discriminated the test sets. Image set "Small" stands out the most for critic scores and morphological metrics. For the "Small" set, smaller particles received a higher count in the local thickness, volume fractions were

calculated smaller, and interfacial line length larger than for the other image sets. The degree of differentiation between "Pristine," "Medium," and "Large" varied depending on applied measure. Interestingly, the order of the image sets was calculated consistently for the critic scores and the morphological metrics.

Test Set 2

Test set 2 probed the sensitivity of the critic to particle shape variations. From **Figure 11,** we can deduce that the critic does not distinguish particle shape well. There was a slight shift of the score distribution to smaller scores for the "Swirl" images but there was no appreciable shift for "Polar" and "Wave." The calculation of the volume fraction responded similarly. "Swirl" images also produced the largest differences in local thickness and interfacial line length compared to the "Pristine" reference (training set 1). While easily distinguishable by the human eye, the shape changes introduced by image transformations were difficult for the critic to track and did not significantly influence morphological metrics related to performance. For energetic material applications this insensitivity of the critic may be a desired attribute and worth further exploration.

Test Set 3

Test set 3 assessed the ability of the computational approaches to identify subtle morphological change due to aging of Pharmatose. These changes are difficult for the human analyst to detect. **Figure 12** reveals that the critic scores were shifted to higher scores for images of the aged material and that the interfacial line length decreased with age. When these observations are compared with those made for test set 1 (varying particle size), it suggests that aging increases particle size. This seems reasonable since particle aggregation due to aging with corresponding specific surface area (3-dimensional equivalent to interfacial line length) decrease and particle size increase has been observed before.[19, 20] The local thickness changed only slightly but the portion of larger particles also appeared to increase with age. However, the volume fraction decreased for the aged image sets, while it increased for larger particles (test set 1). Further analysis may be warranted.

ANTICIPATED OUTCOMES AND IMPACTS:

We showed that the critic of a GAN can be used as a detector of morphological change in image data. This was a proof-of-principal study that lays the foundation for the development of an automated, quantitative, and consistent tool for image analysis within surveillance. Our interest is energetic material surveillance, where image analysis is currently performed manually. However, such a tool would be material agnostic. CT scans produce large amounts of data and an automated tool would greatly improve the efficiency of subsequent image analysis. Moreover, quantitative image analysis allows for the detection of trends and the application of machine learning

algorithms to discover structure/property relationships that are not possible with manual, qualitative image analysis.

We hope that our investigation will inspire future work to improve the sensitivity of the critic. Better sampling (i.e., larger training images) should narrow distributions. An improved generator architecture (more layers, filters) might help with the recognition of particle boundaries to avoid the occurance of fused particles. Alternative training strategies, where occasionally an out-of-distribution image is shown to the critic, might also be considered to mitigate the insensitivity of the critic to particle shape if this is desired.

In this project, we used CT data with documented magnification. Data was collected from consistently prepared material in aging vehicles. An obstacle that is common to the application of machine learning/deep learning methods to image data is the variation in the images due to instrument settings and sampling method. This can be fairly well controlled for CT imaging, where all the material in the container is scanned at once. However, the GAN-based image analysis developed here may also be extended to other imaging techniques, such as scanning electron microscopy (SEM). For SEM, sample preparation can introduce undesired image variations. For instance, the sample may be scanned at different angles or material might be placed on a different support. Material sampling also affects image content. Often the analyst selects a material sample where signs of aging are suspected or most likely. A prerequisite for a successful appliaction of a machine learning/deep learning tool is the development of a standardized imaging protocol. We plan to implement a consistent SEM imaging strategy for pristine and aged CL-20 and/or PETN samples for a future Aging & Lifetime project, which would then allow us to train the GAN on SEM image data and test the ability of the critic to detect morphological change in SEM image data.

An immediate follow-on project would be the use of PETN and CL-20 pristine and aged CT data sets that are currently being produced within the Aging & Lifetime program. The goal would be to understand if, and how, shifts in score distributions correlate to time and/or temperature of accelerated aging.

The generation of realistic images has a potentially impactful application since it allows for microstructure control [9] without resolving to oversimplified models. Fitted 2-dimensional pore models yield tunable microstructurs that can be used as input to shock-physics codes to study the relationship between microstructure and response to shock loading [21]. However, the input structures lack realism. Realistic CT images may also be used as input for shock-physics codes but without the ability to vary the microstructure. Using the trained GAN to generate input images has the unique advantage of providing realistic and tunable microstructures, permitting targeted energetic material design.

The GAN is capable of processing 3-dimensional images. Training with 3-dimensional images should enhance the sensitivity of the critic. However, current memory limitations hinder training with more than approximately 300,000 pixels (flattened vector), which is equivalent to a cube

length of less than 70 pixels. Strategies are developed at Sandia in the context of other work [22] that reduce memory requirements. For extension to 3D, a collaboration is recommended.

This work was orally presented at the 2022 Machine Learning/ Deep Learning Workshop at Sandia on July 27th 2022. The title of the presentation was "Utilization of the Critic Subnetwork of a Generative Adversarial Network as Detector of Morphological Material Change in Image Data".

A manuscript with title "Utilization of the Critic Subnetwork of a Generative Adversarial Network as Detector of Morphological Material Change in Image Data" has been prepared for submission to a special issue (invitation only) of *Propellants, Explosives, Pyrotechnics* that is focused on data science and machine learning relevant to energetic materials. The manuscript will be submitted in FY22.

CONCLUSION:

We investigated the ability of the critic of a GAN to detect out-of-class images displaying a change in morphology versus the morphology shown in the images with which the GAN had been trained. Train and test images were CT images of Pharmatose, which is used in our laboratory as a surrogate for energetic materials.

Because critic and generator are trained together, we first evaluated generated images. Visually, the microstructure of Pharmatose was replicated well, although we observed sporadic, unrealistic particle fusion. We also compared morphological metrics for train (real) and synthetic images focusing on metrics that correlated to performance of energetic materials. We calculated volume fraction and local thickness that were reproduced well in the synthetic images. Volume fraction relates to density and local thickness to particle size distribution. The interfacial line length (2-dimensional equivalent to specific surface area) showed bimodal characteristics in the training images. While this was not reflected in the synthetic images, the calculated interfacial line length of the generated images approximately peaked at the average location of the bimodal features. Mode collapse is not uncommon in GANs. [18]

We found that the critic can distinguish images of pristine Pharmatose from images of Phamatose that have different particle sizes. Scores are ordered consistently with respective morphological metrics. However, variations in particle shape that appear considerable to the human eye are difficult for the critic to detect. The introduced shape variations do not cause considerable morphological metric changes either. By contrast, the critic, as well as morphological metric analysis, recognized images of aged Pharmatose that the human eye could hardly discriminate from pristine material. We note that while network training is time consuming, it is only required once; interrogation of the critic is much faster than morphological metric analysis.

REFERENCES:

1. Wildenschild, D. and A.P. Sheppard, *X-ray imaging and analysis techniques for quantifying pore-scale structure and processes in subsurface porous medium systems.* Advances in Water Resources, 2013. **51**: p. 217-246.
2. Torquato, S., *Statistical description of microstructures.* Annual Review of Materials Research, 2002. **32**: p. 77-111.
3. Russakovsky, O., et al., *ImageNet Large Scale Visual Recognition Challenge.* International Journal of Computer Vision, 2015. **115**(3): p. 211-252.
4. Goodfellow, I., et al., *Generative Adversarial Networks.* Communications of the Acm, 2020. **63**(11): p. 139-144.
5. Gayon-Lombardo, A., et al., *Pores for thought: generative adversarial networks for stochastic reconstruction of 3D multi-phase electrode microstructures with periodic boundaries.* Npj Computational Materials, 2020. **6**(1).
6. Mosser, L., O. Dubrule, and M.J. Blunt, *Reconstruction of three-dimensional porous media using generative adversarial neural networks.* Physical Review E, 2017. **96**(4).
7. Mosser, L., O. Dubrule, and M.J. Blunt, *Stochastic Reconstruction of an Oolitic Limestone by Generative Adversarial Networks.* Transport in Porous Media, 2018. **125**(1): p. 81-103.
8. Hsu, T., et al., *Microstructure Generation via Generative Adversarial Network for Heterogeneous, Topologically Complex 3D Materials.* Jom, 2020.
9. Chun, S., et al., *Deep learning for synthetic microstructure generation in a materials-by-design framework for heterogeneous energetic materials.* Scientific Reports, 2020. **10**(1).
10. Fokina, D., et al., *Microstructure synthesis using style-based generative adversarial networks.* Physical Review E, 2020. **101**(4).
11. Arjovsky, M., S. Chintala, and L. Bottou, *Wasserstein GAN.* arXiv:1701.07875 [stat.ML], 2017.
12. Brereton, R.G., *One-class classifiers.* Journal of Chemometrics, 2011. **25**(5): p. 225-246.
13. *Scikit-Image, Version 0.19.1; Open source software,* . Available from: https://scikit-image.org/docs/dev/index.html.
14. Dinegar, R.H., R.H. Rochester, and M.S. Millican, *EFFECT OF SPECIFIC SURFACE ON THE SHOCK SENSITIVITY OF PRESSED GRANULAR PETN*. 1962, ; Los Alamos Scientific Lab., N. Mex. p. Medium: X; Size: Pages: 8.
15. Gifford, M.J., P.E. Luebcke, and J.E. Field, *A new mechanism for deflagration-to-detonation in porous granular explosives.* Journal of Applied Physics, 1999. **86**(3): p. 1749-1753.
16. Hildebrand, T. and P. Ruegsegger, *A new method for the model-independent assessment of thickness in three-dimensional images.* Journal of Microscopy-Oxford, 1997. **185**: p. 67-75.
17. *PoreSpy, Version 2.0.2; Open source software,*. Available from: https://porespy.org/user_guide/index.html.
18. Arora, S. and Y. Zhang, *Do GANs actually learn the distribution? An empirical study.* arXiv:1706.08224v2 [cs.LG], 2017.
19. Maiti, A., et al., *In-situ Monitoring of Flow-Permeable Surface Area of High Explosive Powder using Small Sample Masses.* Propellants Explosives Pyrotechnics, 2015. **40**(3): p. 419-425.

20. Maiti, A., et al., *Long-term Coarsening and Function-time Evolution of an Initiator Powder.* Propellants Explosives Pyrotechnics, 2017. **42**(12): p. 1352-1357.
21. Yarrington, C.D., R.R. Wixom, and D.L. Damm, *Shock interactions with heterogeneous energetic materials.* Journal of Applied Physics, 2018. **123**(10).
22. Potter, K.M., et al., *Automatic detection of defects in high reliability as-built parts using X-Ray CT.* Applications of Machine Learning 2020, 2020. **11511**.